Journal of Materials Chemistry C

Accepted Manuscript

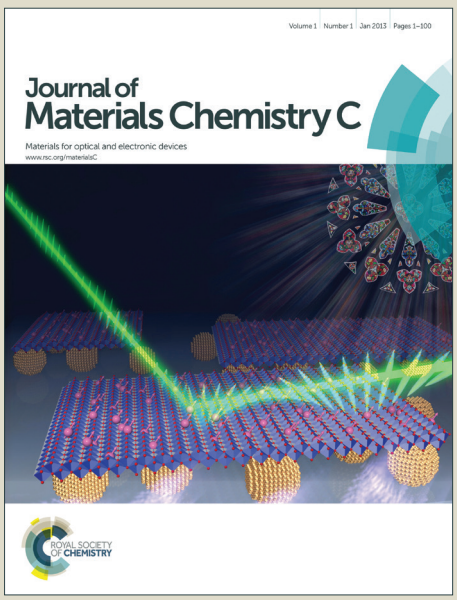

ROYAL SOCIETY OF CHEMISTRY

www.rsc.org/materialsC

Magnetostructural phase transformations in $Tb_{1-x}Mn_2$

Junding Zou,*[ab] Durga Paudyal,[b] Jing Liu,[bc] Yaroslav Mudryk,[b] Vitalij K. Pecharsky[bc] and Karl A. Gschneidner, Jr.[bc]

[a] *School of Materials Science and Engineering, Zhejiang University, Hangzhou, Zhejiang 310027, China. E-mail address: zoujd@zju.edu.cn. Tel: 86-571-87952366.*

[b] *The Ames Laboratory, US Department of Energy, Iowa State University, Ames, Iowa 50011-3020, USA*

[c] *Department of Materials Science and Engineering, Iowa State University, Ames, Iowa 50011-2300, USA*

Magnetism and phase transformations in non-stoichiometric $Tb_{1-x}Mn_2$ (x=0.056, 0.039) have been studied as functions of temperature and magnetic field using magnetization, heat capacity, and x-ray powder diffraction measurements. Upon lowering the temperature, the compounds sequentially order ferrimagnetically and antiferromagnetically, and finally, exhibit spin reorientation transitions. Structural distortions from room temperature cubic to low temperature rhombohedral structures occur at T_N, and are accompanied by large volume changes reaching ~-1.27% and -1.42%, respectively. First principles electronic structure calculations confirm the phase transformation from the ferrimagnetic cubic structure to the antiferromagnetic rhombohedral structure in $TbMn_2$.

1. Introduction

Large localized magnetic moments, strong single ion anisotropies, and complex magnetic order are typical features observed in many intermetallic compounds that contain lanthanides. Among numerous known families of metallic materials, systems that contain manganese in addition to the rare earth(s) may exhibit unusual and, therefore, interesting magnetic properties. The magnetic moments of Mn atoms depend on the nature of a material, and they may be either localized or itinerant. All known types of magnetic exchange interactions have been reported for various Mn-based compounds, e.g., direct exchange, double exchange, super exchange, as well as indirect Ruderman-Kittel-Kasuya-Yosida (RKKY) exchange interactions.[1] Colossal magnetoresistance,[2,3] giant magnetocaloric effect (MCE),[4,5,6,7] phase separation,[8] and magnetic frustration[9] have been reported in the past. The intricacy and complexity of magnetic interactions for many of the systems containing both R (R = rare earth) and Mn is well represented by the family of RMn_2 compounds, which has been studied in the past, but even today, magnetic and structural behaviors of this system are not completely understood.

The RMn_2 compounds with R = Pr, Nd, Er, Tm, and Lu crystallize in the C14 type structure (hexagonal $MgZn_2$-type, space group $P6_3/mmc$), while those with R=Y, Sm, Gd, Tb, Dy, and Ho may crystallize in either the C15 type structure (cubic $MgCu_2$-type, space group $Fd\bar{3}m$) or the C14 type structure depending on the sample preparation conditions.[10,11] RMn_2 compounds show different magnetic behaviors, including ferromagnetic (FM), ferrimagnetic (FIM), heliferromagnetic (HFM), and canted

antiferromagnetic (AFM) ordering. Large magneto-volume effects have been observed in RMn_2 compounds with R = Y, Pr, Nd, Sm, Gd, Tb at the respective Néel temperatures, T_N.[10-23] It has been suggested that there is a critical Mn-Mn distance (d_c=2.66 Å) below which the magnetic moment of Mn becomes unstable.[24] Therefore, large magneto-volume effects may be associated with the instability of Mn magnetism.[12,13]

Lattice parameter of the C15-type phase (which determines the Mn-Mn interatomic distances) can be used to estimate whether the Mn atom has a magnetic moment in RMn_2 compounds: when $d_{Mn-Mn} > 2.66$ Å, the moment is present but when $d_{Mn-Mn} < 2.66$ Å, then there is no moment on the Mn atom. This simple model, which is based on the nearest neighbor distances, cannot explain the coexistence of Mn atoms with non-zero and zero moments when the cubic structure undergoes a distortion during the magnetic phase transition.[18] Such behavior is usually referred to as the mixed magnetic phase, and it likely originates from the fact that these compounds are geometrically frustrated systems since Mn atoms form highly symmetrical [Mn_4] tetrahedra in the Laves phase structures. To reduce the geometrical frustration in the ordered state, the Mn atoms in one of the two symmetrically non-equivalent atomic sites in the rhombohedrally distorted polymorph can become non-magnetic. Consequently, the ordered state is a compromise between the magnetic and crystal structures in which some magnetic atoms lose (or reduce) their magnetic moments,[18,25,26] and the crystal structure undergoes a distortion. [14-16,18,27]

Depending on the preparation method (e.g., melting at ambient or high pressure), $TbMn_2$ crystallizes in either the C15 or C14 type structures at room temperature.[11] The

compound with the C15 structure undergoes a first-order phase transition at the Néel temperature (T_N ~45 K), during which a ~1.6% volume discontinuity may be observed, but the magnitude of the volume change is sample dependent.[12,17,19-22] The large volume change is associated with the structural distortion from the high temperature cubic structure to the low temperature rhombohedral structure (space group $R\bar{3}m$).[18] A large hysteresis at the first-order phase transition is observed in both neutron scattering and magnetostriction measurements.[18,20] In addition, the time-of-flight neutron powder diffraction data indicated a possibility of a monoclinic (space group *C2/m*) distortion in $TbMn_2$.[28] Somewhat surprisingly, the reported shape of specific heat anomaly at T_N is λ-type, in contrast to the δ-type expected for the first-order phase transitions, which is a unique feature considering such a large volume change.[22,29]

The unit cell of $TbMn_2$ compounds with the cubic C15 structure is shown in Fig. 1(a). Tb atoms occupy 8a sites, and Mn atoms occupy 16d sites. The Mn atoms form a three-dimensional network of corner-sharing tetrahedra. This topology of magnetic atoms may result in spin frustrations and competing magnetic interactions. The frustrations can be reduced by a structural distortion at Néel temperature from the cubic to rhombohedral structure.[18] Figure 1(b) shows the low temperature rhombohedral structure (space group $R\bar{3}m$). The space group $R\bar{3}m$ is a subgroup of $Fd\bar{3}m$. The Tb atoms occupy 6c sites, and Mn atoms occupy 3b (Mn1) and 9e (Mn2) sites, respectively (see Table 1 for the refined structural parameters). The three-dimensional network of corner-sharing tetrahedra formed by the Mn atoms occupying two symmetrically inequivalent atomic positions is preserved, but the tetrahedra become slightly distorted as a result of the loss

of cubic symmetry. The neutron diffraction study of single crystal $TbMn_2$ suggested several magnetic structures that develop as a function of temperature: a ferromagnetic-like phase between 40 and 45 K, an incommensurate AFM structure with the main propagation vector $\left[\frac{2}{3}\frac{2}{3}0\right]$ below 40 K, and another AFM phase at 2 K characterized by a second propagation vector $\left[\frac{1}{2}\frac{1}{2}\frac{1}{2}\right]$ in both Mn and Tb sublattices.[18] The magnetic structure of $TbMn_2$ changes with the application of magnetic field. The microscopic low temperature magnetic structure of $TbMn_2$ in high magnetic field is illustrated in Fig. 7 of Ref. 18. However, the origin of the complex magnetic state and its relationship with the lattice distortion remain unknown.

A brief review of earlier studies given above indicates several opportunities for further advancements of basic science of this intermetallic system. First, all of the previous studies were performed on nominally stoichiometric alloys without probing for deviations from stoichiometry, which is a common feature in many of the C15-type Laves phases.[30] As we show below, $TbMn_2$ is indeed stable over a narrow but non-negligible homogeneity range, Second, the characteristics of complex magnetic states in $TbMn_2$ need to be probed in-depth experimentally, including crystallographic, magnetic, and heat capacity measurements. Third, the coupling mechanism between Mn and Tb atoms, the details of the electronic structure, and the nature of Tb 5*d*-Mn 3*d* hybridization need to be understood. Here, we address these fundamental issues by performing systematic

experimental measurements for two nonstoichiometric $Tb_{1-x}Mn_2$ complemented by first principles electronic structure calculations on $TbMn_2$.

2. Experimental

Nonstoichiometric polycrystalline samples of $Tb_{1-x}Mn_2$ were prepared by induction melting of pure metals. The Tb metal was obtained from the Materials Preparation Center of the Ames Laboratory and was 99.99 wt.% pure with respect to all other elements in the Periodic Table.[31] The purity of Mn was 99.9 wt. %. Excess amounts of Mn (7.5 at % for x=0.056, and 2 at. % for x=0.039) were added. The metals were sealed in tantalum crucibles in a helium atmosphere. The mixture was melted at 1650 K and held for 24 mins; cooled down to 1200 K and held at this temperature for 1 hr; further cooled down to 1120 K (holding for 2 hrs); then cooled down to 970 K (holding for 2 hrs) before finally powering off the induction furnace.

The single phase $Tb_{1-x}Mn_2$ samples with C15 cubic structure were observed by x-ray diffraction (XRD) study at room temperature performed on a Philips PANalytical powder diffractometer employing monochromatic Cu $K\alpha_1$ radiation. Small amounts of Tb_6Mn_{23} in $Tb_{0.944}Mn_2$ and Tb in $Tb_{0.961}Mn_2$ were observed in the backscattering scanning electron microscope (SEM) measurements (Figs 2a, 2b), and were confirmed by energy dispersive spectroscopy (EDS) analysis. These results indicate that all peritectic reactions have been completed in $Tb_{0.961}Mn_2$, and practically completed in $Tb_{0.944}Mn_2$. The temperature dependent XRD measurements were carried out on a Rigaku TTRAX rotating anode

powder diffractometer equipped with helium flow cryostat[32] (Mo $K\alpha$ radiation). The crystallographic parameters were determined by performing Rietveld refinement of the collected XRD patterns using Rietica-LHPM.[33] The dc and ac magnetization measurements were performed using magnetic property measurement system (MPMS) from Quantum Design Inc. The magnetic hysteresis loops of powder samples and heat capacity measurements were conducted on a physical property measurement system (PPMS) from Quantum Design Inc.

3. Results and discussion

According to previous reports,[30,34,35] rare earth-deficient Laves phase compounds can exist, sometimes forming complex superstructures, but over the range of concentrations studied in this work, $TbMn_2$ preserves the cubic C15-type structure. Figure 2(c) shows fragments of the room temperature XRD patterns of $Tb_{1-x}Mn_2$ in the vicinity of the (113) Bragg peak of the cubic structure, which exhibits a shift of 0.059° as the non-stoichiometry with respect to the Tb concentration increases. The extent of Tb deficiency and stoichiometry of the Laves phases in two alloys has been determined by the EDS analysis and confirmed by Rietveld refinement. The cubic lattice parameter a calculated by Rietveld refinement increases from 7.6352(2) Å for $Tb_{0.944}Mn_2$ to a = 7.6558(3) Å for $Tb_{0.961}Mn_2$ (see Table 1). Lattice parameters of $TbMn_2$ reported in the past range from 7.60 to 7.65 Å.[18, 36, 37] Considering that the unit cell parameter of our least defect alloy (which also contains a minor amount of Tb impurity) is nearly identical to the upper bound of previously reported values, it is likely that none of the earlier reported samples

were stoichiometric. The temperature dependent powder XRD measurements confirm that $Tb_{1-x}Mn_2$ undergo structural transformations[18] at low temperatures. For example, Fig. 2(d) shows that the (222) Bragg peak of the cubic structure in $Tb_{0.944}Mn_2$ splits into (006) and (202) peaks, both representing rhombohedral structure below T_N, and Fig. 2(e) illustrates changes in Bragg scattering as a function of temperature in the vicinity of these Bragg peaks. Figure 2(f) shows that the (044) Bragg peak of the cubic structure in $Tb_{0.961}Mn_2$ splits into (208) and (220) rhombohedral peaks below T_N, and Fig. 2(g) shows details in the vicinity of these Bragg reflections as a function of temperature. The crystallographic information obtained from the Rietveld refinements of the XRD patterns of $Tb_{1-x}Mn_2$ measured at 15 K is also listed in Table 1. The Mn atoms occupy 3b (Mn1) and 9e (Mn2) sites in the rhombohedral structure, and form a network of slightly distorted corner-sharing tetrahedra. For $Tb_{0.944}Mn_2$, $d_{Mn1\text{-}Mn2}$ = 2.6849(2) Å and $d_{Mn2\text{-}Mn2}$ = 2.6904(2) Å at 15 K. For $Tb_{0.961}Mn_2$, $d_{Mn1\text{-}Mn2}$ and $d_{Mn2\text{-}Mn2}$ are 2.6992(2) and 2.6895(2) Å, respectively, at 15 K. The Mn-Mn distances exceed the critical distance (d_c=2.66 Å, below which the Mn moment becomes unstable) in both the high temperature cubic and low temperature rhombohedral polymorphs of the two compounds.[24] No other structural transformations are observed down to 5 K.

Figure 3 shows the temperature dependence of lattice parameters and unit-cell volumes of $Tb_{0.944}Mn_2$ and $Tb_{0.961}Mn_2$ in the vicinity of AFM↔FIM and FIM↔PM phase transitions determined during heating in zero magnetic field. For $Tb_{0.944}Mn_2$, the first-order AFM↔FIM phase transition that occurs around 39 K is accompanied by a change in the *a* parameter ($\Delta a/a$ = −0.49%), a smaller change in the *c* parameter ($\Delta c/c$ = -0.27%), and

the unit cell volume change $\Delta V/V$ is −1.27%. The second-order FIM-PM phase transition occurs around 49 K, and is also accompanied by anomalies in the unit cell dimensions. For $Tb_{0.961}Mn_2$, the region between the first-order AFM↔FIM (T_N=46 K) and second-order FIM-PM (T_C=54 K) phase transitions is narrower, and a similar change in the *a* parameter ($\Delta a/a$ = −0.40%) is accompanied by a much larger change in the *c* parameter ($\Delta c/c$ = -0.60%); the unit cell volume change $\Delta V/V$ is −1.42%. In both compounds, large and discontinuous phase volume changes are associated with the AFM-FIM transformations, while only minor and continuous lattice anomalies are observed at the FIM-PM transitions

The temperature dependent magnetization measured in different magnetic fields is shown in Fig. 4. The zero-field-cooling (ZFC) and field-cooling (FC) data show that $Tb_{1-x}Mn_2$ compounds undergo multiple magnetic phase transitions: a second order PM↔FIM phase transition at the Curie temperature, T_C, a first order FIM↔AFM phase transition at the Néel temperature, T_N, and a spin reorientation (SR) transition at T_{SR}. The two main transformations at T_C and T_N have been reported in the past, but the transition at T_{SR} has not been reported before. For clarity, T_C and T_N are also marked in Figs. 2(e) and 2(g). According to the temperature dependent magnetization measured in high magnetic fields, the AFM ordering temperature, T_N, shifts to lower temperature and T_{SR} shifts to higher temperature when the magnetic field increases. Noticeable thermal irreversibilities are observed between ZFC and FC measurements just below T_C in 100 Oe, while thermal irreversibilities only occur below T_N in higher magnetic fields. Unusual crossovers of ZFC and FC magnetization curves are observed in 10 kOe for $Tb_{0.944}Mn_2$ and in both 100

Oe and 10 kOe field for $Tb_{0.961}Mn_2$ due to SR transitions. Only a single FIM transition is seen in the magnetization data of $Tb_{0.944}Mn_2$ in 50 kOe, while both the AFM↔FIM and FIM↔PM transitions remain discernible for $Tb_{0.961}Mn_2$ in a 50 kOe magnetic field. It seems that the Tb atomic vacancies are beneficial to AFM↔FIM transition in low temperature, and AFM↔FIM transition is much easier to occur in $Tb_{0.944}Mn_2$ than $Tb_{0.961}Mn_2$.

Figure 5 shows real and imaginary components of ac magnetic susceptibility measured in a zero bias dc magnetic field on heating at two different frequencies, 1 and 100 Hz with 5 Oe driving ac field. The ac magnetic susceptibility shows sharp asymmetric peaks which are similar to that reported for a single crystal of $TbMn_2$.[38] Energy losses as indicated by the non-zero imaginary components of the magnetic susceptibility (not shown) confirm the formation of domain structure at the FIM transition; energy losses become nearly negligible at and below the AFM transformations. This result further supports the FIM ordering at T_C. Moreover, frequency dependent behaviors were observed in two temperature regions: between T_C and T_N (the inset of Fig. 5) and around T_{SR}, respectively. The insets of Fig. 5 show that with increasing frequency the ac magnetic susceptibility slightly decreases between T_N and T_C. Similarly, Fig. 5 shows that with increasing frequency the ac susceptibility is also reduced around T_{SR}. We note here that commonly, frequency dependent ac magnetic susceptibility is reflective of spin glass behavior. Further, similar frequency dependent behavior observed in $(Dy_{0.4}Y_{0.6})Mn_2$ and $(Dy_{0.4}Y_{0.6})Al_2$ compounds was assumed to be related to a spin glass freezing transition.[39] However, as follows from earlier neutron scattering data,[18] the title materials preserve

long range magnetic order down to 2 K. Hence, this rather unusual frequency dependence of the ac magnetic susceptibility most likely points to the existence of magnetic clustering.

Figure 6 shows the magnetic hysteresis loops measured at different temperatures in ZFC conditions. The initial magnetization curves cross the magnetic hysteresis loops, which is especially obvious at low temperatures. This is unusual because in most cases the initial magnetization curve does not cross the magnetic hysteresis loop. Similar feature was observed in Dy_5Si_3Ge compound,[40] but $Tb_{1-x}Mn_2$ show much larger discrepancies. This behavior may originate from non-equilibrium states during the phase transition. Furthermore, it should be noted that the initial magnetization curves in $Tb_{1-x}Mn_2$ are not linear with the magnetic field as expected for an antiferromagnetically ordered system. With the magnetic field increasing, both the initial magnetization curves and the magnetic hysteresis loops show a number of step-like features. Considering the dc and ac susceptibilities, all of these phenomena indicate that the field-induced phase transitions accompanied by non-equilibrium phase separation behavior may exist in $Tb_{1-x}Mn_2$.

Figure 7 shows the coercivity, H_c, of $Tb_{1-x}Mn_2$ as a function of temperature. As expected, H_c decreases with increasing temperature, but it anomalously increases from 730 Oe at 19 K to 970 Oe at 25 K for $Tb_{0.944}Mn_2$. A small anomaly is also observed at 25 K for $Tb_{0.961}Mn_2$. These anomalous changes of coercivity suggest that modification of magnetic anisotropy occurs in the vicinity of these temperatures. In many cases, rare-earth anisotropy contribution dominates at low temperatures, whereas a small anisotropy in the

vicinity of a magnetic phase transition point is determined by the contributions from transition-metal sublattice.[41] The magnetic anisotropy in $Tb_{1-x}Mn_2$ is likely determined by both Tb and Mn, thus leading to the SR transitions because the ordering temperatures of both compounds are quite low.

Figure 8 shows the heat capacity measured as a function of temperature in different magnetic fields. For $Tb_{0.944}Mn_2$ in zero magnetic field, a first anomaly corresponding to FIM ordering is observed at T_C = 49 K and a second sharp peak corresponding to the AFM ordering is observed at T_N = 40 K. No obvious anomaly is observed around T_{SR} in zero magnetic field, but a small anomaly is observed around T_{SR} = 31 K in 10 kOe magnetic field, as shown in the inset of Fig. 8(a). In addition, a spike in the heat capacity is observed between T_C and T_N in a zero magnetic field, which reflects a measurable range of temperatures over which the coupled AFM-FIM/structural transformation is completed due to a large volume change. Heat capacity measurements show less sharp anomalies in 10 kOe and 20 kOe. T_C and T_N of $Tb_{0.961}Mn_2$ are 54 and 47 K, respectively. A spike is also observed between T_C and T_N under zero magnetic field, but it disappears with the increasing magnetic field. Different from $Tb_{0.944}Mn_2$, a minor but noticeable anomaly is observed at T_{SR} = 26 K in $Tb_{0.961}Mn_2$ even in a zero magnetic field. Compared with $Tb_{0.961}Mn_2$, the heat capacity anomalies of $Tb_{0.944}Mn_2$ that reflect AFM-FIM and structural transitions remain broad in non-zero magnetic field due to different phase transition widths, weakening of first-order phase transition, and overlapping structural, AFM-FIM, and SR transitions. The application of magnetic field shifts the T_N and T_{SR}

downward and upward, respectively. T_C does not shift with the magnetic field suggesting a second order phase transition.

Finally, we note that the influence of Tb_6Mn_{23} or Tb impurities observed in SEM images (figure 2a,b) on the magnetism and observed phase transformations of the title materials is negligible because: 1) their concentrations are lower than the limit of detection using x-ray diffraction (usually a few vol. %), and 2) the magnetic transitions in Tb and Tb_6Mn_{23} occur at temperatures far away from the magnetic phase transitions in $Tb_{1-x}Mn_2$ regardless of x. Specifically, Tb orders magnetically at T_C = 221 K and T_N = 229 K, [42] and the Curie temperature of Tb_6Mn_{23} is 457 K. A weak metamagnetic behavior observed [43] in phase-pure Tb_6Mn_{23} below 30 K is not reflected in the isothermal magnetization data of $Tb_{0.944}Mn_2$ shown in Fig. 6 due to the low concentration of the former.

4. Theoretical investigation

Manganese is a 3*d* element, which has either broad or narrow 3*d* bands depending on the alloy or compound it forms with other elements. In metallic compounds Mn typically exhibits itinerant magnetism through spin polarized 3*d* bands. Terbium, on the other hand, has narrow or localized 4*f* and broad conduction electron (*spd*) bands. Its magnetic moment is a sum of 6 μ_B from 4*f* spins and 3 μ_B from the 4*f* orbital moment contribution. In addition to indirect 4*f*-4*f* exchange interactions, crystal field splitting may also play a significant role in Tb. It is, therefore, challenging but interesting to understand the

interplay between Tb 4*f*, Tb 5*d*, and Mn 3*d* electrons in the Laves phase $TbMn_2$ compound.

For simplicity, we employ a stoichiometric $TbMn_2$ model, i.e. disregarding the presence of minor defects on Tb sites. The local spin density approximation including Hubbard U parameter (LSDA+U) approach [44] has been employed to investigate the electronic structure and magnetic properties of $TbMn_2$. Our calculations have been performed using the scalar relativistic version (which includes the mass velocity and Darwin correction terms) of the LSDA+U method implemented in the tight binding linear muffin tin orbital (TB-LMTO) approach.[45] In order to check the effect of full potential in $TbMn_2$, we have also employed the full potential linear augmented plane wave (FP-LAPW) method with LSDA+U.[46] FP-LAPW showed results similar to TB-LMTO, indicating that TB-LMTO method is suitable for $TbMn_2$. Therefore, the results shown below are from LSDA+U within TB-LMTO calculations. The electronic structure calculations performed with different values of Hubbard *U* ranging from 1 eV to 7 eV indicate that when *U* increases, the spin up states are shifted to the lower energy while the spin down states are shifted to the higher energy, as expected. Below we show the calculations with U=6.7 eV and J=0.7 eV, the well-known values of Gd, considering similar energy difference between the occupied and unoccupied 4*f* states in Gd and Tb. Furthermore we have used 145 and 417 special k points in the irreducible part of the Brillouin zone for k space integration of cubic and rhombohedral structures, respectively.

The spin polarized FIM (initial approximation with Tb spins up and Mn spins down) calculations show that the total energy of the rhombohedral $TbMn_2$ is lower than that of the cubic polymorph by 1.17 eV, confirming the former as the ground state structure, in which the magnetic moments of Mn (3b) and Mn (9e) have opposite signs, (see next paragraph). Figure 9 shows Tb 4*f* density of states (DOS) in both the rhombohedrally distorted and the cubic structures. The crystal field split spin up 4*f* DOS are located between -6 and -7 eV in the rhombohedral $TbMn_2$. The spin down 4*f* bands are also split: one band is at the Fermi level and the other two are much higher. The calculated 4*f* spin moment of Tb in the rhombohedral $TbMn_2$ is 5.83 μ_B/Tb. The total Tb moment including the 4*f* orbital moment is 8.83 μ_B/Tb, which agrees well with 8.70 μ_B/Tb observed from neutron diffraction.[18] The nearly degenerate spin up 4*f* states of Tb in the cubic $TbMn_2$ are located at ~-9 eV. The spin down 4*f* bands are split: one is at the Fermi level and the other is at ~2 eV. This leads to 6.11 μ_B/Tb 4*f* spin moment (9.11 μ_B/Tb total moment). The instability of the cubic structure is related to the sharp peak in the spin down 4f band, which dominates the total DOS (also see Fig. 10) and is absent in the rhombohedral polymorph.

Figure 10 shows 3*d* (5*d*) DOS of Mn (Tb) atoms in both $TbMn_2$ structures. In the rhombohedral structure, the magnetic moments of Mn (3b) and Mn (9e) are different: -2.46 μ_B and 0.29 μ_B, respectively. The opposite magnetic moments on Mn atoms are surprising since it is well-known that the 4*f* moments of the heavy lanthanides align antiparallel to the 3*d* moments of the transition metal. A neutron powder diffraction study with molecular field analysis[18] suggests two arrangements of Mn moments in the

rhombohedral FIM structure, both of which give identical magnetic intensities: in the first, 0.3 μ_B are present on each site, in the second, only the (3b) site is magnetic with 1.37 μ_B at 5 K, while the (9e) site carries no moment. Our calculations, therefore, favor the second of the two models, especially considering that the estimated error in the calculated moment is on the order of 0.05 μ_B. In the cubic $TbMn_2$ the magnetic moment of Mn is -0.69 μ_B/Mn, which is antiparallel to the Tb moments as expected.

5. Conclusions

In this study, we have identified the existence of nonstoichiometric $Tb_{1-x}Mn_2$ (x=0.056, 0.039) compounds, and characterized their magnetic, structural, and thermodynamic properties. The x-ray powder diffraction measurements demonstrate that these Laves phase compounds undergo a rhombohedral distortion at T_N accompanied by large volume changes of -1.27% and -1.42%, respectively. The magnetization and heat capacity measurements show multiple magnetic transitions: FIM at T_C, AFM at T_N, and SR at T_{SR}. T_N and T_{SR} shift downward with reduction of the Tb content. The large volume changes are not simply related to the development of the magnetic moment of Mn atoms, but to the first-order AFM↔FIM magnetostructural phase transition. The magnetic anisotropy in $Tb_{1-x}Mn_2$ is determined by both of Tb and Mn, and anomalously modified leading to the SR transition. The electronic structure calculations confirm the rhombohedral distortion as the ground state crystal structure in $TbMn_2$, and reveal the sharp peak in the spin down 4f band that leads to instability of the cubic structure.

Acknowledgments

This work was supported by the National Natural Science Foundation of China (Grant No. 51471150). Work at the Ames Laboratory was supported by the U.S. Department of Energy, Office of Basic Energy Science, Division of Materials Sciences and Engineering. The research was performed at the Ames Laboratory operated for the U. S. Department of Energy by Iowa State University under Contract No. DE-AC02-07CH11358.

Notes and references

1 M. Donath, and W. Nolting (Eds), in *Local-Moment Ferromagnets*, (Springer, Berlin Heidelberg, 2005).

2 R. von Helmolt, J. Wecker. B. Holzapfel, L. Schultz, and K. Samwer. *Phys. Rev. Lett.* 1993, **71**, 2331.

3 S. Jin, T. H. Tiefel, M. McCormack, R. A. Fastnacht, R. Ramesh, and L. H. Chen, *Science* 1994, **264**, 413.

4 H. Wada, and Y. Tanabe, *Appl. Phys. Lett.* 2001, **79**, 3302.

5 J. D. Zou, H. Wada, B. G. Shen, J. R. Sun, and W. Li, *Europhys. Lett.* 2008, **81**, 47002.

6 O. Tegus, E. Bruck, K. H. J. Buschow, F. R. de Boer, *Nature* 2002, **415**, 150.

7 W. L. Zuo, F. X. Hu, J. R. Sun, and B. G. Shen, *J. Alloys and Compd.* 2013, **575**, 162.

8 M. Uehara, S. Mori, C. H. Chen, and S.-W. Cheong, *Nature* (London) 1999, **399**, 560.

9 R. Ballou, C. Lacroix, and M. D. Nunez Regueiro, *Phys. Rev. Lett.* 1991, **66**, 1910.

10 M. Shiga, *Physica B* 1988, **149**, 293.

11 K. Inoue, Y. Nakamura, A. V. Tsvyashchenko, and L. Fomicheva, *J. Phys. Soc. Jpn.* 1995, **64**, 2175.

12 M. Shiga, H. Wada, and Y. Nakamura, *J. Magn. Magn. Mater.* 1983, **31-34**, 119.

13 Y. Nakamura, *J. Magn. Magn. Mater.* 1983, **31-34**, 829.

14 Y. Tagawa, J. Sakurai, Y. Komura, H. Wada, M. Shiga, and Y. Nakamura, *J. Phys. Soc. Jpn.* 1985, **54**, 591.

15 I. Yu. Gaidukova, V. V. Kelarev, A. S. Markosyan, A. Z. Menshikov, and A. N. Pirogov, *J. Magn. Magn. Mater.* 1988, **72**, 357.

16 R. Cywinski, S. H. Kilcoyne, and C. A. Scott, *J. Phys.: Condens. Matter* 1991, **3**, 6473.

17 R. Ballou, I. Yu. Gaydukova, A. S. Markosyan, and B. Ouladdiaf, *J. Magn. Magn. Mater.* 1992, **104-107**, 1465.

18 P. J. Brown, B. Ouladdiaf, R. Ballou, J. Deportes, and A. S. Markosyan, *J. Phys.: Condens. Matter* 1992, **4**, 1103.

19 M. R. Ibarra, C. Marquina, L. Garcia-Orza, and A. del Moral, *Solid State Commun.* 1993, **87**, 695.

20 E. Lelievre-Berna, J. Rouchy, and R. Ballou, *J. Magn. Magn. Mater.* 1994, **137**, L6.

21 C. Marquina, M. R. Ibarra, C. de la Fuente, A. del Moral, *J. Magn. Magn. Mater.* 1995, **140-144**, 809.

22 M. Shiga, and H. Wada, *J. Magn. Magn. Mater.* 1995, **151**, 225.

23 H. Yamaoka, N. Tsujii, I. Jarrige, Y. Takahashi, J. Chaboy, H. Oohashi, K. Handa, J. Ide, T. Tochio, Y. Ito, T. Uruga, and H. Yoshikawa, *Phys. Rev. B* 2009, **80**, 115110.

24 K. Yoshimura, M. Shiga, and Y. Nakamura, *J. Phys. Soc. Jpn.* 1986, **55**, 3585.

25 C. Ritter, S. H. Kilcoyne, and R. Cywinski, *J. Phys.: Condens. Matter* 1991, **3**, 727.

26 C. Ritter, R. Cywinski, S. H. Kilcoyne, and S. Mondal, *J. Phys.: Condens. Matter* 1992, **4**, 1559.

27 H. Nakamura, N. Metoki, S. Suzuki, F. Takayanagi, and M. Shiga, *J. Phys.: Condens. Matter* 2001, **13**, 475.

28 S. Mondal, R. Cywinski, S. H. Kilcoyne, B. D. Rainford, and C. Ritter, *Physica B* 1992, **180&181,** 606.

29 Z. Tarnawski, L. Kolwicz-Chodak, H. Figiel, A. Budziak, L. Havela, J. Vejpravova, A. Kolomiets, V. Sechovsky, and N.-T. H. Kim-Ngan, *Physica B* 2005, **355**, 202.

30 K. A. Gschniedner, Jr., and V. K. Pecharsky, *Z. Kristallogr.* 2006, **221**, 375.

31 Materials Preparation Center, Ames Laboratory US-DOE, Ames, IA, USA, [www.mpc.ameslab.gov].

32 A. P. Holm, V. K. Pecharsky, K. A. Gschneidner, R. Rink, and M. N. Jirmanus, *Rev. Sci. Instrum.* 2004, **75**, 1081.

33 B. Hunter, Rietica-*A Visual Rietveld Program, International Union of Crystallography Commission on Powder Diffraction Newsletter*, No. 20 (Summer, 1998), [http://www.rietica.org.]

34 V. Paul-Boncour, A. Percheron-Guegan, M. Diaf, and J. C. Achard, *J. Less-Common Met.* 1987, **131**, 201.

35 D. J. Thoma, and J. H. Perepezko, *J. Alloys Compd.* 1995, **224**, 330.

36 A. S. Ilyushin, W. E. Wallace, *J. Solid State Chem.* **1976**, 17, 373.

37 K. Shimizu, *J. Phys. Soc. Jpn.* **1985**, 54, 1154.

38 E. Talik, M. Kulpa, T. Mydlarz, J. Kusz, H. Bohm, and A. Winiarski, *Physica B* 1999, **271**, 265.

39 J. R. Stewart, J. M. Hillier, P. Manuel, and R. Cywinski, *J. Phys.: Condens. Matter* 2011, **23**, 164205.

40 R. Nirmala, Ya. Mudryk, V. K. Pecharsky, and K. A. Gschneidner, Jr., *Phys. Rev. B* 2007, **76**, 104417.

41 R. Skomski, and J. M. D. Coey, in *Permanent Magnetism*, edited by J. M. D. Coey, (Institute of Physics Publishing, Bristol and Philadelphia, 1999), Vol. 1, Chap. 3, p.135-150.

42 V. I. Zverev, A. M. Tishin, A. S. Chernyshov, Ya. Mudryk, K. A. Gschneidner Jr. and V. K. Pecharsky, *J. Phys.: Condens. Matter* 2014, **26**, 066001.

43 P. Lemoine, A. Vernière, T. Mazet, B. Malaman, J. Magn. Magn. Mater. 2011, 323, 2690.

44 V. I. Anisimov, F. Aryasetiawan, and A. I. Lichtenstein, *J. Phys.: Condens. Matter* 1997, **9**, 767.

45 O. K. Andersen, and O. Jepsen, *Phys. Rev. Lett.* 1984, **53**, 2571.

46 P. Blaha, K. Schwarz, G. Madsen, D. Kvasnicka, and J. Luitz, WIEN2k, An Augmented Plane Wave plus Local Orbitals Program for Calculating Crystal Properties (Austria: Karlheinz Schwarz, Techn. Universität Wien), 2001

Table 1. Crystal structure parameters of $Tb_{1-x}Mn_2$ at room temperature (RT) and 15 K[a], respectively.

	atom	x/a	y/b	z/c	$B_{overall}$ (Å^2)	occupancy
$Tb_{0.944}Mn_2$ @RT	Tb	1/8	1/8	1/8	0.32(1)	0.953(2)
	Mn	1/2	1/2	1/2	0.32(1)	1
S.G. $Fd\bar{3}m$		a=7.6352(2)Å, V=445.10(2) Å^3,				
		Rp=3.08%, Rwp=4.19%, Rexp=3.04%, χ=1.90				
$Tb_{0.944}Mn_2$ @15 K	Tb	0	0	0.1233(4)	0.47(4)	0.953
	Mn1	0	0	0.5	0.47(4)	1
	Mn2	0.5	0	0	0.47(4)	1
S.G. $R\bar{3}m$		a=5.3807(3) Å, c=13.140 (1) Å, V=329.47 (4) Å^3				
		Rp=13.23%, Rwp=6.63%, Rexp=3.40%, χ=3.80				
$Tb_{0.961}Mn_2$ @ RT	Tb	1/8	1/8	1/8	0.79 (8)	0.960(2)
	Mn	1/2	1/2	1/2	0.79 (8)	1
S.G. $Fd\bar{3}m$		a=7.6558(3) Å, V=448.72(3) Å^3				
		Rp=4.33%, Rwp=5.43%, Rexp=6.06%, χ=0.80				
$Tb_{0.961}Mn_2$ @15 K	Tb	0	0	0.1246(6)	0.9(1)	0.960
	Mn1	0	0	0.5	0.9(1)	1
	Mn2	0.5	0	0	0.9(1)	1
S.G. $R\bar{3}m$		a=5.3790(3) Å, c=13.247(1) Å, V=331.93(5) Å^3				
		Rp=14.87%, Rwp=9.57%, Rexp=2.38%, χ=16.23				

[a] Larger residuals compared to room temperature data are related to the fact that the low temperature data have been measured using consolidated samples without spinning (see Ref. 32), while the room temperature data have been collected using loose powdered

specimens which were continuously spun. Thus, intensities of the low temperature powder patterns are less representative of an “ideal” powder diffraction pattern.

Figure captions:

FIG.1. (Color online) Unit cells of cubic (a) and rhombohedral (b) polymorphs of $TbMn_2$. The large black circles represent Tb atoms, and the small blue and red circles represent Mn1 and Mn2 atoms, respectively. For clarity, only the shortest Mn-Mn bonds are shown.

FIG. 2. (Color online) (a) Backscattering SEM image for $Tb_{0.944}Mn_2$. (b) Backscattering SEM image for $Tb_{0.961}Mn_2$. (c) XRD patterns of $Tb_{1-x}Mn_2$ in the vicinity of the (113) cubic Bragg peak at room temperature (Cu $K\alpha_1$ radiation). (d) XRD patterns in the vicinity of the (222) cubic Bragg peak of $Tb_{0.944}Mn_2$ at 60 K (cubic structure) and 35 K (rhombohedral structure) (both Mo $K\alpha_1$ and $K\alpha_2$ Bragg peaks are present). (e) The contour plot showing the change of Bragg scattering in $Tb_{0.944}Mn_2$ with temperature measured on heating. (f) XRD patterns in the vicinity of the (044) cubic Bragg peak of $Tb_{0.961}Mn_2$ at 60 K (cubic structure) and 35 K (rhombohedral structure). (g) The contour plot showing the change of Bragg scattering in $Tb_{0.961}Mn_2$ with temperature measured on heating. T_C and T_N marked in (e) and (g) correspond to critical temperatures determined from magnetization data measured on heating, also see Fig. 4.

FIG. 3. (Color online) Temperature dependence of the lattice parameters and the unit-cell volumes of (a) $Tb_{0.944}Mn_2$ and (b) $Tb_{0.961}Mn_2$ in the vicinity of AFM↔FIM and FIM↔PM phase transitions determined during heating in zero magnetic field. T_C and T_N are marked. The unit cell dimensions of the cubic unit cell are represented in an idealized rhombohedral unit cell for easy comparison.

FIG. 4. (Color online) Temperature dependences of magnetization of $Tb_{1-x}Mn_2$ compounds. (a)-(b) The ZFC (closed red symbols) and FC (open black symbols) temperature dependences of magnetization of $Tb_{0.944}Mn_2$ measured in 100 Oe, 10 kOe, and 50 kOe applied magnetic fields. (c)-(d) The same for $Tb_{0.961}Mn_2$.

FIG. 5. (Color online) The real and imaginary components of ac magnetic susceptibility measured as a function of temperature and frequency during heating of zero-field-cooled sample. The upper insets clarify behaviors in the range immediately below T_C.

FIG. 6. (Color online) The magnetic hysteresis loops of $Tb_{1-x}Mn_2$ measured at different temperature in ZFC conditions. The initial magnetization curves are marked in red.

FIG. 7. (Color online) The coercivity of $Tb_{1-x}Mn_2$ as a function of temperature.

FIG. 8. (Color online) The heat capacity of $Tb_{1-x}Mn_2$ as a function of temperature at different magnetic fields. The insets enlarge the regions in the vicinities of SR transitions in 10 kOe magnetic field.

FIG. 9. (Color online) The 4*f* density of states of Tb atoms of the cubic Laves phase, and rhombohedrally distorted AFM $TbMn_2$.

FIG. 10. (Color online) The 5*d* DOS of terbium and 3*d* DOS of manganese atoms in the rhombohedrally distorted (a) and cubic Laves phase (b) of FIM $TbMn_2$.

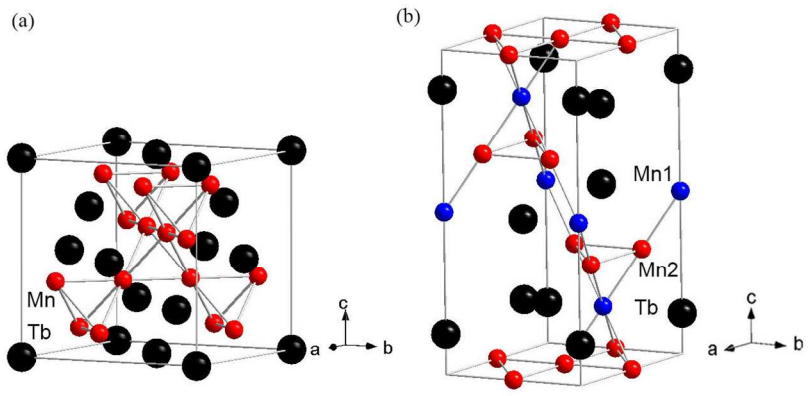

FIG.1

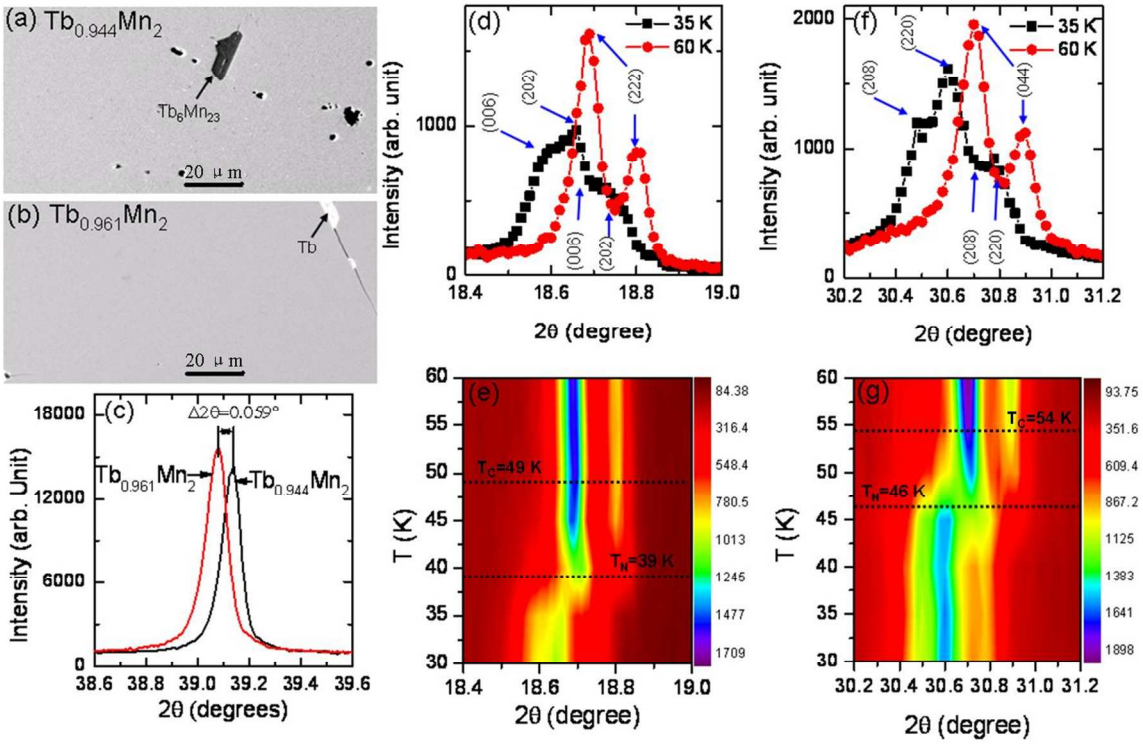

FIG.2

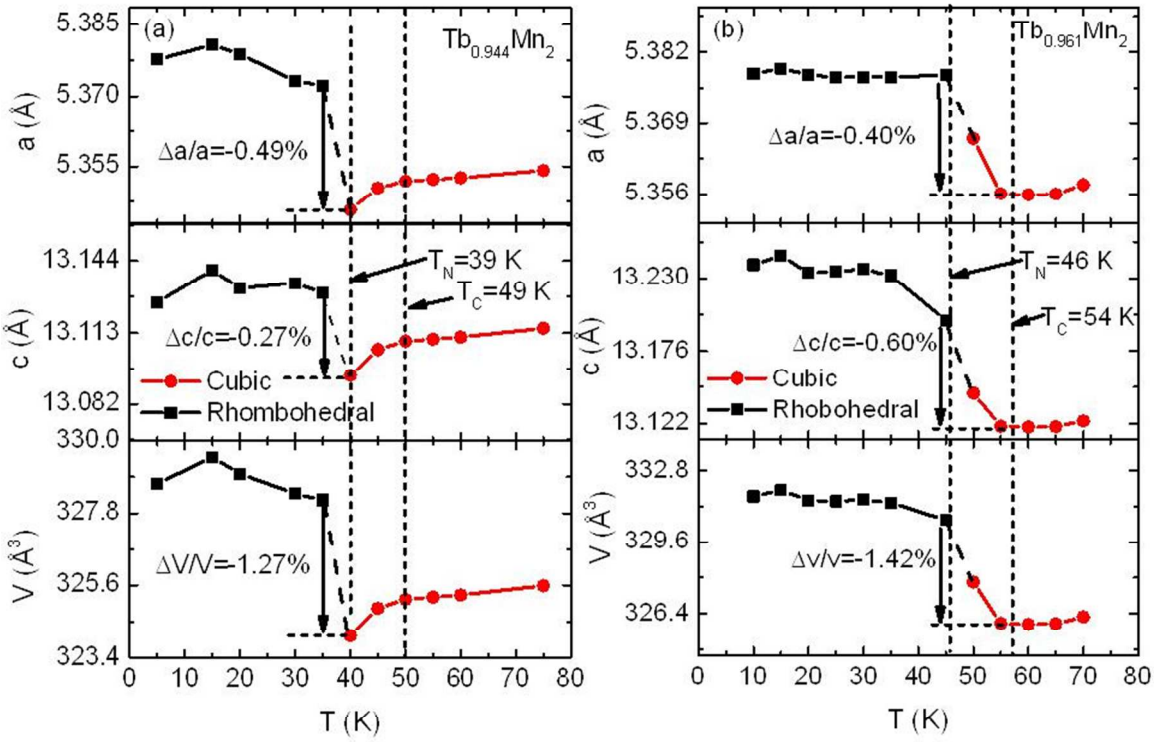

FIG.3

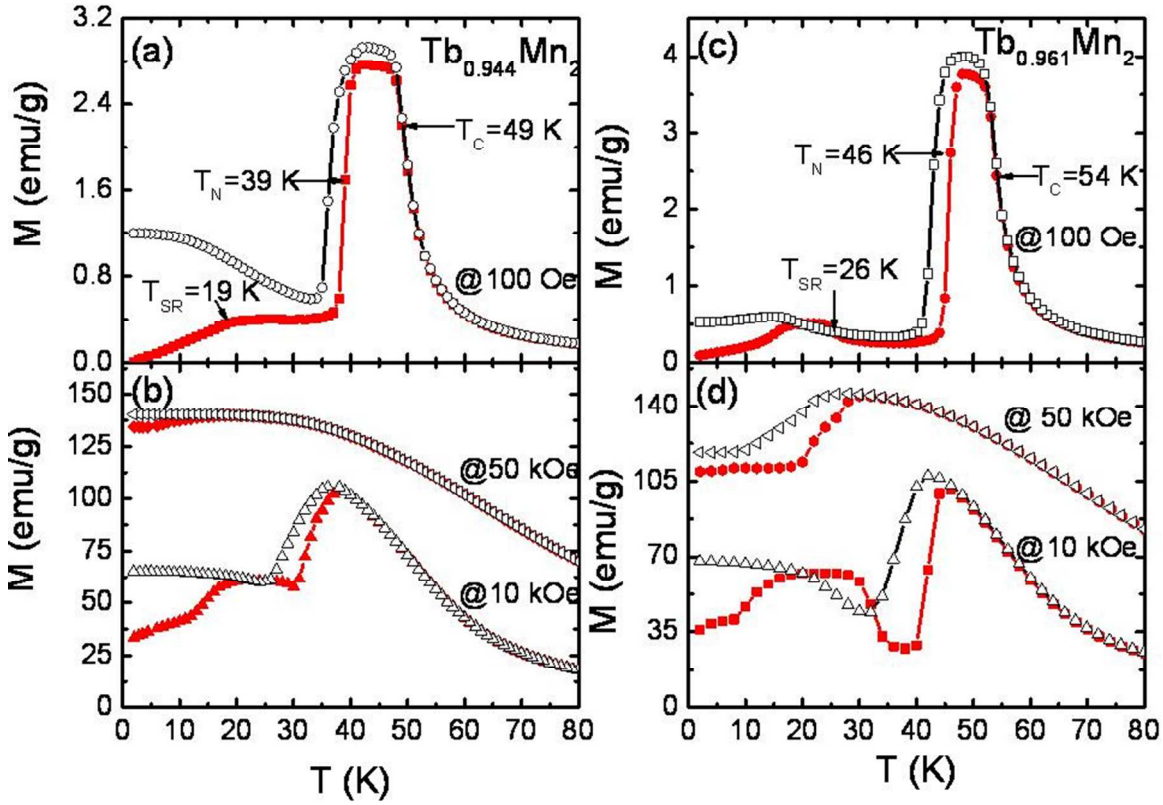

FIG.4

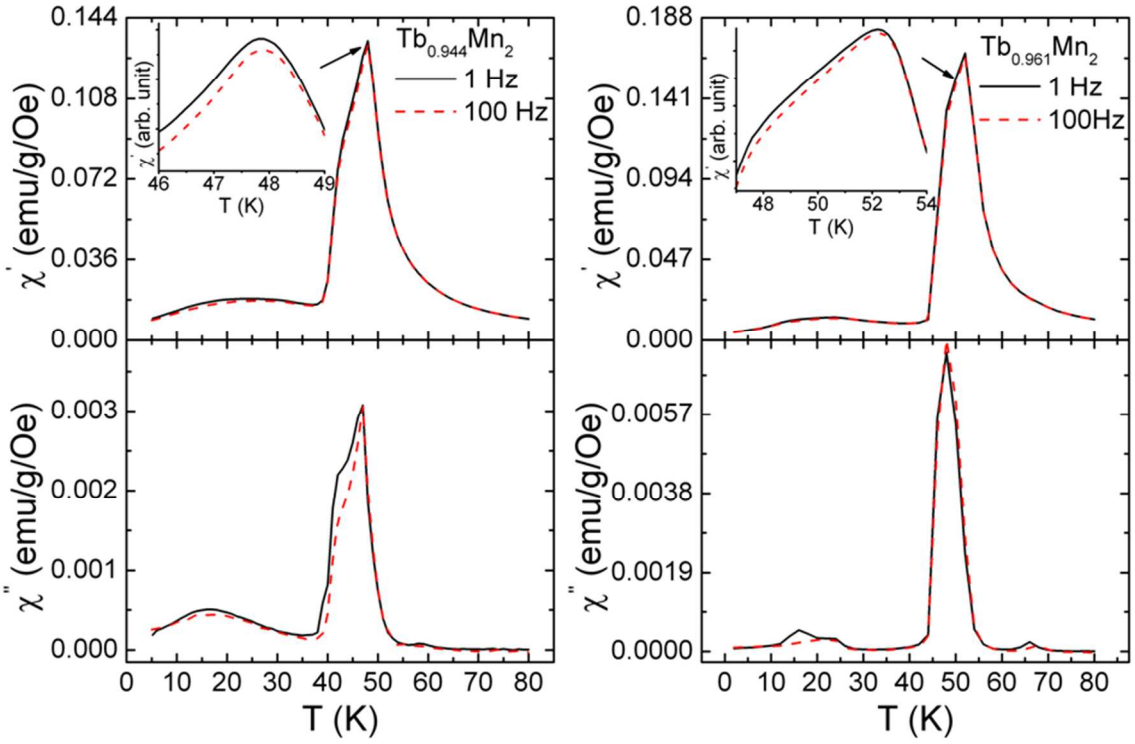

FIG.5

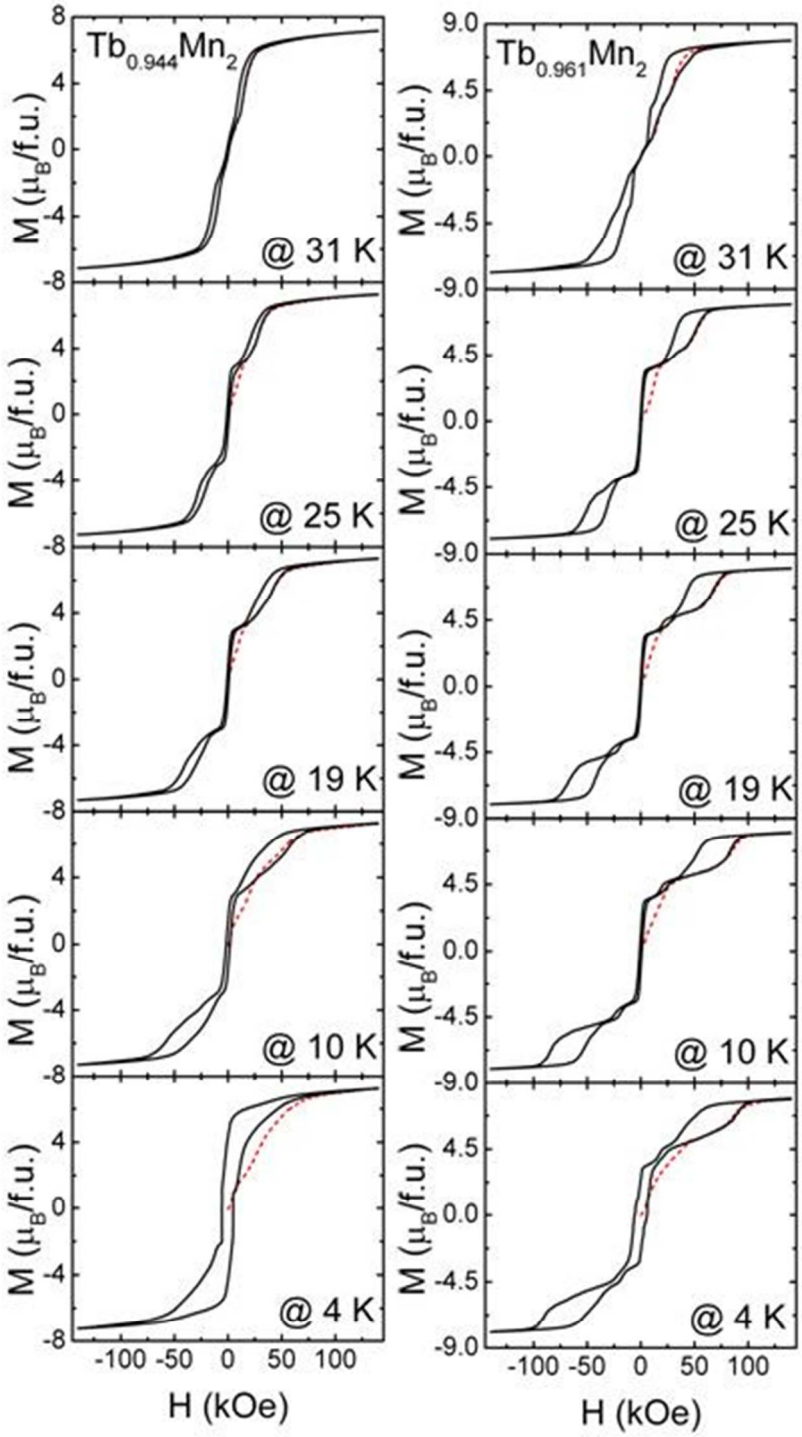

FIG.6

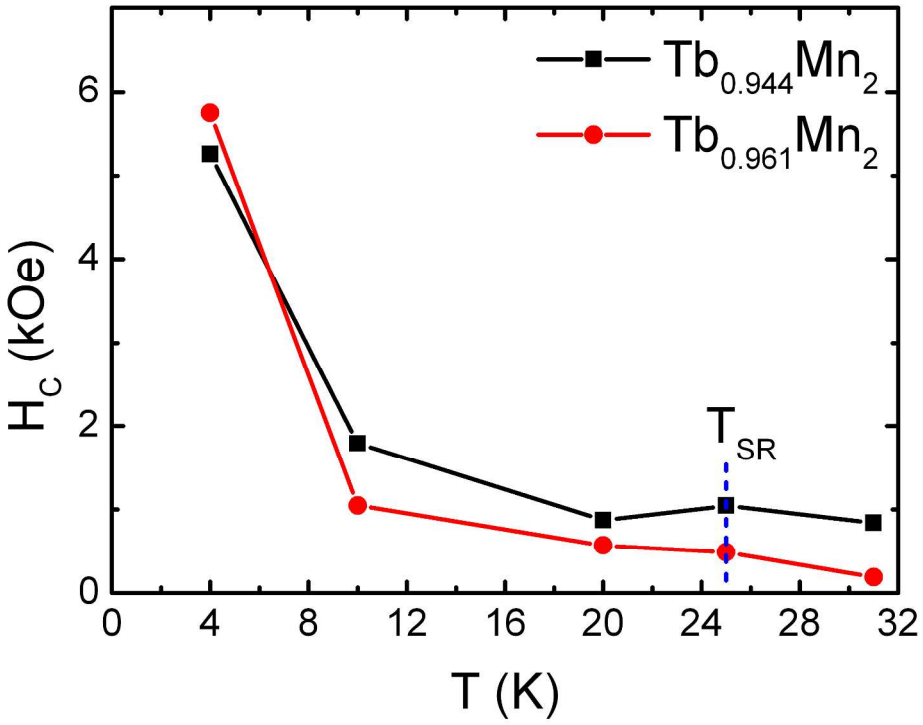

FIG.7

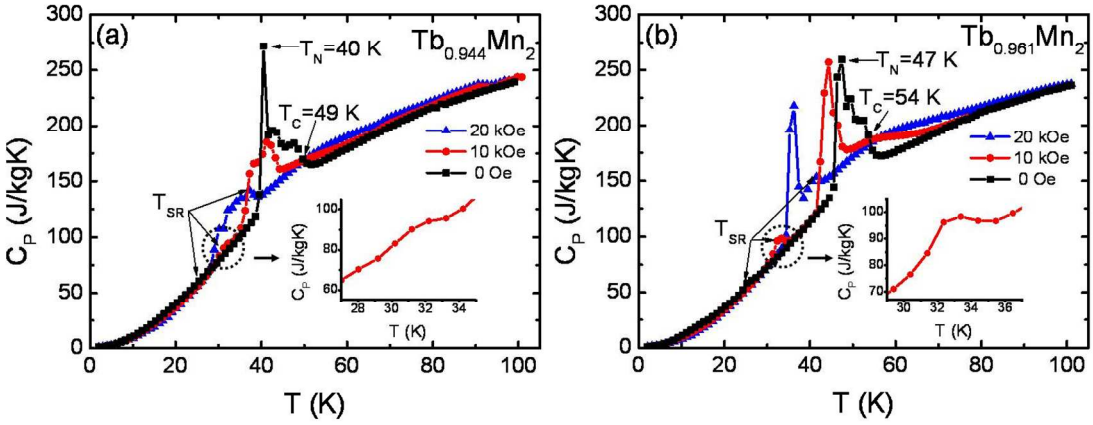

FIG.8

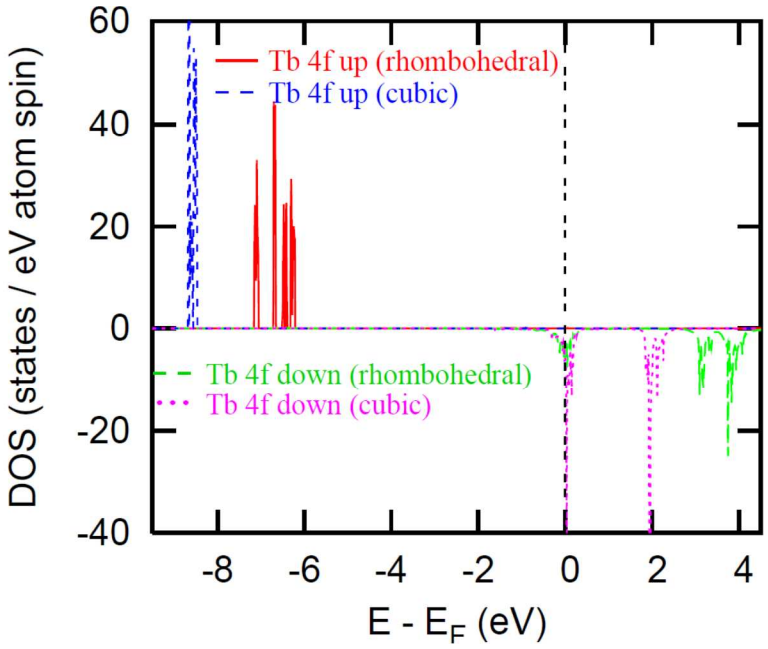

FIG.9

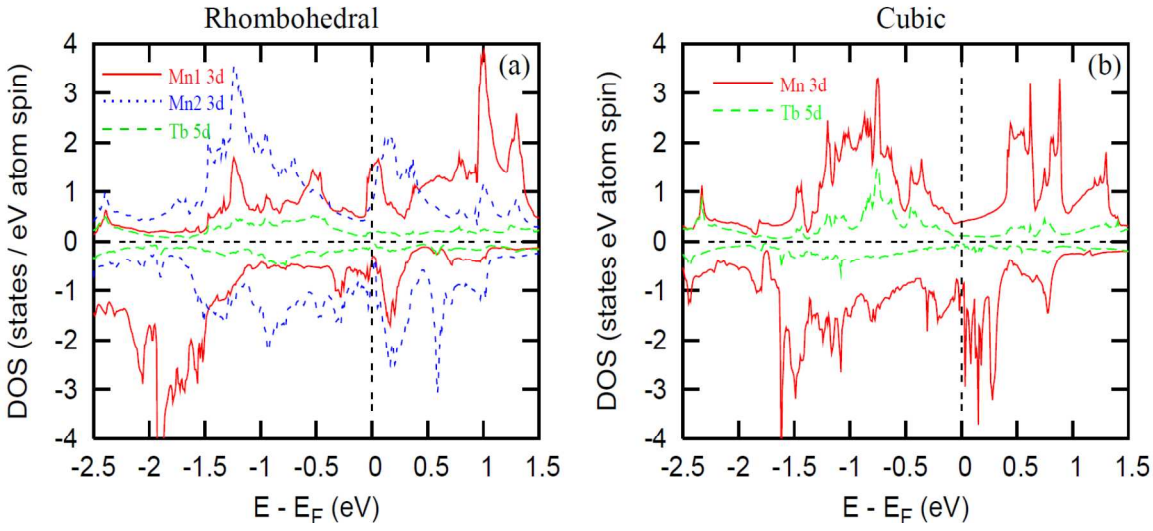

FIG.10

Magnetism and phase transformations in non-stoichiometric $Tb_{1-x}Mn_2$ (x=0.056, 0.039) have been studied as functions of temperature and magnetic field.